2017

Mechanical characterization of parts produced by ceramic on-demand extrusion process

Amir Ghazanfari, *Missouri University of Science and Technology*
Wenbin Li, *Missouri University of Science and Technology*
Ming C. Leu, *Missouri University of Science and Technology*
Gregory E. Hilmas, *Missouri University of Science and Technology*

MR. AMIR GHAZANFARI (Orcid ID : 0000-0003-1197-6327)

Received Date : 14-Dec-2016

Revised Date : 14-Dec-2016

Accepted Date : 18-Jan-2017

Article type : Article

Mechanical characterization of parts produced by ceramic on-demand extrusion process

Amir Ghazanfari*, Wenbin Li, Ming C. Leu

Department of Mechanical and Aerospace Engineering, Missouri University of Science and Technology, Rolla, MO, 65409

Jeremy L. Watts, Gregory E. Hilmas

Department of Materials Science and Engineering, Missouri University of Science and Technology, Rolla, MO, 65409

* amir.ghazanfari@mst.edu

Ceramic On-Demand Extrusion (CODE) is an additive manufacturing process recently developed to produce dense three-dimensional ceramic components. In this paper, the properties of parts produced using this freeform extrusion fabrication process are described. High solids loading (~60 vol%) alumina paste was prepared to fabricate parts and standard test methods were employed to examine their properties including density, strength, Young's modulus, Weibull modulus, toughness, and hardness. Microstructural evaluation was also performed to measure the grain size and critical flaw size. The results indicate that the properties of parts surpass most other ceramic additive manufacturing processes and match conventional fabrication techniques.

Keywords: mechanical properties; aluminum oxide; Al_2O_3; ceramic on demand extrusion; extrusion-based additive manufacturing.

1. Introduction

Additive Manufacturing (AM) of advanced ceramics has several advantages over traditional processing techniques including ease of fabricating geometrically complex parts and reduction of manufacturing costs for one-of-a-kind parts or small batches. Accordingly, many researchers have either modified existing AM processes, which were designed to fabricate polymer components, for fabrication of ceramic components, or invented novel AM technologies specifically for ceramics. The former includes Selective Laser Sintering [1], Stereolithography [2], Three-Dimensional Printing [3], Ink-jet Printing [4], Laminated Object Manufacturing [5], and Fused Deposition of Ceramics [6]. The latter includes Extrusion Freeform Fabrication [7], Robocasting [8], and Freeze-form Extrusion Fabrication [9]. A comprehensive review on additive manufacturing of ceramic-based materials was recently published by Travitzky et al. [10].

Many efforts to additively manufacture ceramic components resulted in parts with defects (i.e., flaws or large porosity as a result of the AM process). It is well-known that the properties of ceramics are very sensitive to porosity, and they would be expected to exhibit poor mechanical properties even at 80% relative density (e.g., [11]). Although these parts may have remarkable geometrical complexity and be suitable for some applications, they are not apt to be used as structural ceramics. In many cases, the mechanical properties of these parts are so poor that they are not even reported in papers and technical reports. According to Zocca et al. [12], AM of monolithic ceramics, enabling the components to match the physical and chemical properties of their

conventionally manufactured counterparts, is still a challenge and remains the most important task that needs to be solved to promote AM of ceramics to more than a niche technology. However, extrusion-based and lithography-based AM processes are promising because they are capable of producing dense ceramic parts (>95% of theoretical density).

The Ceramic On-Demand Extrusion (CODE) process is a novel freeform extrusion fabrication technique capable of making large, complex parts with near theoretical density (>98%). Ghazanfari et al. [13] introduced and developed this process and employed it to demonstrate fabricating several sample parts for various applications. The objective of the present study is to comprehensively characterize ceramic parts produced using the CODE process. Density, strength, fracture toughness, hardness, stiffness and microstructure of aluminum oxide (Al_2O_3) parts were examined and compared to the properties of Al_2O_3 parts fabricated using conventional manufacturing and other AM processes.

2. Experimental Procedure

2.1. Paste Preparation

The paste is made of a commercially available alumina powder (A-16SG, Almatis Inc., Leetsdale, PA), deionized water, ammonium polymethacrylate (DARVAN® C-N, Vanderbilt Minerals, Norwalk, CT), and cold-water-dispersible methylcellulose (Methocel J5M S, Dow Chemical Company, Midland, MI). The powder properties are listed in Table 1.

The alumina powder was dispersed in water using 1 mg Darvan C per square meter of surface area of powder and ball-milled for 15 hours to break up agglomerates and to produce a uniform mixture. Methylcellulose dissolved in water (<1 vol%) was used as a binder to increase paste viscosity and to assist in forming a stronger green body after drying. Binder was chemically surface-treated by the manufacturer to become temporarily insoluble in cold water. This time-delay in dissolving the binder allows for the formation of a homogeneous dispersion of binder in cold water and eliminates the necessity to increase water temperature to achieve a uniform dispersion. A vacuum mixer (Model F, Whip Mix, Louisville, KY) was employed to mix the paste homogeneously without introducing air bubbles for 12 minutes. Finally, a vibratory table (Syntron Material Handling, Saltillo, MS) was used to remove the remaining air bubbles.

2.2. Processing

In the CODE process, viscous colloids of ceramic particles are extruded through a circular nozzle at controlled flowrates. The extrusion workhead is mounted on a gantry and can move in the X, Y and Z directions through G & M code commands[†]. The extrudate is deposited on a substrate located in a tank designed to hold a fluid medium. Once the deposition of each layer is completed, a liquid feeding subsystem pumps oil into the tank, surrounding the deposited layer, to preclude undesirable water evaporation from the sides of the deposited layers. The level of the oil is controlled so that it reaches just below the top surface of the part being fabricated. Infrared radiation is then used to uniformly dry the just deposited layer so that the part being fabricated can maintain its shape when the next layers are being deposited to build the part. The part is fabricated in a layer-by-layer fashion by repeating the layered deposition followed by layered radiation drying with an oil surrounding the already deposited layers during the part fabrication process. A schematic of the process is shown in Figure 1. Once the fabrication process is completed, the remaining water content in the fabricated part is removed further by bulk drying to obtain green parts. The post-processing includes removing the binder content at elevated temperatures and then using a ceramic sintering process to obtain a dense part.

The experimental setup consists of a motion subsystem (gantry) capable of moving in three directions, an extrusion head mounted on the gantry and capable of extruding viscous ceramic pastes at controlled flowrates, an oil feeding device capable of controlling the level of the oil in the tank, and an infrared heating subsystem capable of moving the infrared lamp and turning it on and off. The gantry is controlled by a motion card (Delta Tau Data Systems Inc., Chatsworth, CA) whereas all other subsystems are controlled by a real-time control subsystem with LabVIEW (National Instruments Corp., Austin, TX). More details on the CODE system are available from [13] and [14].

Thirty test bars were fabricated using the CODE process to examine the properties of the parts produced by this process. As shown in Figure 2, six bars were printed at a time. The printing was performed in the longitudinal direction of the bars. The as-printed size of the bars was

[†] G & M codes are a set of letters and numbers used to program the movements and other actions (tool change, end of program, etc.) of a CNC machine.

$72 \times 7.8 \times 5.6$ mm^3 in length, width, and height, respectively. The process parameters used to print the bars are given in Table 2.

2.3. Post-Processing

Once the parts were completely formed, the oil bath was drained and the fabricated pieces were dried. Humid drying was used to eliminate the remaining water in the parts. An environmental chamber (LH-1.5, Associated Environmental Systems, Ayer, MA) was employed to control the temperature and humidity during the drying process. After several experiments, 75% relative humidity at 25 °C was determined for the first 4-6 hours of drying. This condition guaranteed safe drying (i.e. no cracks or warpage). After the first stage of drying, the shrinkage ends and higher drying rates could be achieved, without introducing flaws, by increasing the temperature up to ~70 °C.

The binder was then removed through a burnout process. A 1 °C/min heating rate was chosen to avoid large weight reduction rates. The parts were maintained at 450 °C for two hours. The calcined or "brown" parts were then sintered with a heating rate of 5 °C/min in an electric furnace (Deltech Inc., Denver, CO). The parts were then sintered in the same furnace at 1550 °C for 1.5 h followed by cooling to room temperature at a rate of 10 °C/min.

2.4. Tests

The size of the bars was measured with digital calipers after printing, drying, and sintering to calculate the shrinkage rate during the drying and sintering processes. Archimedes' technique was performed to measure the density of the printed parts after sintering. After the dry mass was recorded, samples were saturated by submersion in distilled water under vacuum for ~12 hours. The saturated and suspended masses were then measured to calculate the final density.

Microstructure images were obtained from sections of the sintered test bars using Scanning Electron Microscopy (SEM). Specimens were polished to a 0.25 μm diamond finish using successively finer diamond abrasives with the following scheme: a 220-grit metal-bond diamond grinding disk for 10 min; a 600-grit disk for 10 min; a 1200-grit disk for 10 min; a 3 μm diamond lapping film for 5 min; a 2 μm diamond paste for 40 min; a 1 μm diamond paste for 90 min; and a 0.25 μm diamond paste for 150 min. Thermal etching was used to reveal the grain boundaries by placing the polished specimens in an electric furnace (Deltech Inc., Denver, CO) at 1300 °C for

30 min with a heating and cooling rate of 10 °C/min. A scanning electron microscope (Helios Nanolab 600, FEI, Hillsboro, OR) was employed to observe the specimens at various magnifications ranging from 100-20,000X. The cross-sections of the bars before and after the flexural tests were also observed under an optical microscope (KH-3000, Hirox, Hackensack, NJ) to examine possible flaws.

Four-point bending tests were performed at room temperature according to ASTM C1161 [15] to measure flexural strengths for 24 test specimens. A fully automated surface grinder (Chevalier, FSG-3A818, Santa Fe Springs, CA) was used to machine the specimens to standard "B" bars ($3\times4\times45$ mm^3). The sides and top surface of the bars were machined with a 600-grit diamond abrasive wheel. A 1200-grit wheel was used to grind the tensile surface. The bars were then manually chamfered using a 1200-grit metal-bond diamond grinding disk. Flexural strengths were measured using a fully articulating B-bar fixture with an outer span of 40 mm and an inner span of 20 mm (shown in Figure 3) in a screw-driven instrumented load frame (5881; Instron, Norwood, MA). The crosshead speed was 0.5 mm/min. Weibull modulus was calculated according to ASTM C1239 [16]. Young's modulus was determined using a deflectometer (a linear variable differential transformer) measuring the deflection of the center of the test bar during strength testing as shown in Figure 3.

Fracture toughness was measured by using the chevron-notched beam test specimens in four-point bending with a fully articulating test fixture for configuration A (L=50 mm, B=3 mm, W=4 mm, and a_0=0.8 mm) according to ASTM C1421 [17]. Six test bars were ground to standard size using the same surface grinder employed for flexural tests. The chevron notches were machined using a dicing saw (Accu-cut 5200, Aremco Products, Ossining, NY) with a 0.15 mm thick diamond wafering blade. The same fixture and load frame used for flexural tests were employed to break the chevron-notched beams with a crosshead speed of 0.02 mm/min. The notch dimensions were then measured using an optical microscope (KH-3000, Hirox, Hackensack, NJ).

Vickers indentation test was carried out according to ASTM C1327 [18] using a microhardness tester (Duramin 5; Struers, Cleveland, OH) to measure hardness. Four samples were polished to a 0.25 μm diamond finish using the same scheme explained for microstructural tests. Hardness was calculated from five indents per sample. The indenter was pressed against the parts with a force of 4.91 N for 10 s. The indentation size was measured using an optical microscope with a 40X lens.

3. Results and Discussion

3.1. Shrinkage and Density

The size of the bars reduced to 71×7.5×5.4 mm^3 after drying, showing 1.4%, 3.8% and 3.6% reduction in length, width and height, respectively. This indicates a volumetric shrinkage of 8.6%. The dimensions of the bars were 62.8×6.3×4.6 mm^3 after sintering, showing 12.8%, 19.2% and 17.9% reduction in length, width and height, respectively, compared to the wet (as-printed) samples. This indicates a volumetric shrinkage of 42.1% compared to the wet samples. The results are given in Table 3 along with relative densities.

To examine whether the anisotropy in shrinkage is a result of printing direction or the geometry of the part, three blocks were printed. The initial size of the blocks was 20×19.8×20 mm^3 and it reduced to 16.7×16.6×16.6 mm^3, showing 16.5%, 16.2% and 17.0% reduction in length, width, and height, respectively. This shows an almost isotropic shrinkage and indicates that the percentage of shrinkage in each direction is mostly determined by the part geometry. It is hypothesized that friction between specimen and substrate causes the anisotropy in the shrinkage of long bars during drying and sintering; i.e. due to friction, it is more difficult for particles to move in the longitudinal direction of the bar than in the transverse (or thickness) direction. However, further evidence is required to confirm this conjecture.

3.2. Microstructure

Figure 4 shows a typical microstructure of a printed Al_2O_3 test specimen for a cross-section perpendicular to the printing direction. The grains are equiaxed and small (<5 μm). Grain size was measured by the lineal intercept method. Twenty horizontal lines, with random distances relative to each other, were drawn on the image of microstructure. The length of the lines was equal to the width of the image and each line had 20-30 interceptions with grain boundaries. The grain size was estimated using the following equation.

$$D = 1.56\frac{\sum l_i}{\sum n_i} \quad (1)$$

where D is the average grain size in μm, l_i is the length of each line in μm and n_i is the number of interceptions for each line. An average grain size of 2.1 μm was determined using this method.

3.3. Mechanical Properties

The cumulative distribution function for the Weibull distribution is:

$$P_f = 1 - \exp[-(\frac{\sigma_{max}}{\sigma_\theta})^m] \quad (2)$$

where P_f is the probability of failure, σ_{max} is maximum tensile stress in a test specimen at failure, σ_θ is the Weibull characteristic strength (corresponding to a P_f = 0.632 or 63.2%), and m is Weibull modulus. The procedure in ASTM 1239 [16] was implemented in a Matlab script to fit the function on the raw data, find the Weibull parameters, and obtain the Weibull plot.

The readings of the deflectometer were plugged in Equation (3), which was obtained from Euler-Bernoulli beam theory (see e.g., [19] for an explanation of this theory), to calculate Young's modulus as follows:

$$E = \frac{11Pl^3}{768I\delta} \quad (3)$$

where E is Young's modulus (N/m^2), P is the total load (N), l is the outer span of the fixture (m), I is the second moment of inertia of the test specimen cross-section about the neutral axis (m^4), and δ is the mid-span deflection (m). δ is measured by the deflectometer and P is measured by a load-cell. For a rectangular cross-section with four chamfered edges of size c, the adjusted moment of inertia is given in [15]:

$$I = \frac{bd^3}{12} - \frac{c^2}{9}(c^2 + \frac{(3d-2c)^2}{2}) \quad (4)$$

where b and d are width and height of the bar (m), respectively, and c is the chamfer size (m).

The Weibull plot of the flexural strength data is shown in Figure 5. The Weibull characteristic strength was 385.3 MPa and the raw Weibull modulus was 8.33. According to ASTM 1239 [16], the unbiasing factor for the maximum likelihood estimate of the Weibull modulus when 24 specimens are used is 0.943. Thus, the unbiased Weibull modulus is 7.85. The average flexural strength was 364 MPa with a standard deviation of 50 MPa. Young's modulus was found to be 371±14 GPa. The average values of fracture toughness and hardness were 4.5±0.1 MPa•m$^{0.5}$ and 19.8±0.6 GPa, respectively. All of these values are in good agreement with available data in the literature for

pressureless sintering of alumina produced by conventional methods (e.g., [20–22]). According to these references, a dense fine-grained alumina ceramic has a flexural strength of 300-500 MPa, a Young's modulus of 380-400 GPa, a fracture toughness of 3.5-5 MPa•$m^{0.5}$, and a Vickers hardness of ~20 GPa. Figure 6 shows typical fracture and indented surfaces from the specimens tested in this study.

The Griffith criterion was used to calculate the critical flaw size in each sample. Assuming the flaws are internal (based on observations discussed next), the size of flaws can be calculated using the following equation:

$$2c = 2(\frac{K_{IC}}{\sigma_f Y})^2 \quad (5)$$

where $2c$ is the length of the flaw (m), K_{IC} is the fracture toughness (MPa•$m^{0.5}$), σ_f is the fracture stress (MPa), and Y is the stress intensity shape factor. σ_f is measured at the flaw location, which is assumed to be near the tensile surface. Y is equal to 1.77 and 1.13 for long flaws and round flaws, respectively, according to ASTM C1322 [23]. Thus, the estimated length of the flaw ($2c$) is 102±34 μm for long flaws and 252±84 μm for round flaws.

Figure 7 shows a typical cross-section of printed samples using SEM at a low magnification. No printing flaws were observed in the images of the samples after fabrication. Figure 8 demonstrates two typical fracture origins believed to result from air bubbles or binder agglomerates in the paste. Most fracture surfaces revealed similar flaws near the tensile surface.

Available data in the literature for other additive manufacturing processes were collected for alumina to compare the results of this study with other AM processes. As stated in ASTM 1683 [24], the observed strength values of advanced ceramics are dependent on test specimen size, geometry and stress state. Thus, the procedure explained in the ASTM standard was employed to convert the strength values reported in different sources to the strength of standard "B" bars (3×4×45 mm^3) in order to have a meaningful comparison. Other properties (e.g., modulus, hardness) are not size-dependent and thus the reported values were used in the comparison, even though different test methods and parameters may have affected the results to some extent.

According to ASTM 1683 [24], Equations (6) and (7) can be used to obtain the Weibull material scale parameter from the mean flexural strength and vice versa. Equation (6) is for volume-origin flaws and Equation (7) is for surface-origin flaws (hence the subscripts V and A).

$$(\sigma_0)_V = \frac{\bar{\sigma}_V \left\{ \left(\frac{L_i}{L_o} m_V + 1 \right) \left(\frac{1}{2(m_V+1)^2} \right) V \right\}^{1/m_V}}{\Gamma\left(\frac{1}{m_V} + 1\right)} \quad (6)$$

$$(\sigma_0)_A = \frac{\bar{\sigma}_A \left\{ L_o \left(\frac{d}{m_A+1} + b \right) \left(\frac{L_i}{L_o} m_A + 1 \right) \left(\frac{1}{m_A+1} \right) \right\}^{1/m_A}}{\Gamma\left(\frac{1}{m_A} + 1\right)} \quad (7)$$

where σ_0 is the Weibull material scale parameter, $\bar{\sigma}$ is the mean strength measured in experiments, L_i and L_o are the lengths of inner and outer spans, respectively, m is the Weibull modulus, b and d are the width and height of sample, respectively, V is the gage volume ($b \times d \times L_o$), and Γ is the gamma function.

As mentioned in the Introduction section, the mechanical properties of products of many AM processes of ceramics are poor and researchers often do not report the mechanical properties. However, there are some AM processes capable of producing dense ceramic parts with notable properties. For each of these processes, the highest values reported in the literature are collected and listed in Table 4 for comparison. These processes include Lithography-based Ceramic Manufacturing (LCM) [25], Selective Laser Sintering (SLS) [26], Robocasting (RC) [27], Freeze-form Extrusion Fabrication (FEF) [28,29], Three-Dimensional Printing (3DP) [30], and Binder Jetting (BJ) [31].

It should be noted that in AM processes, the deposition orientation could affect the mechanical properties of the parts to some extent. For example, Huang et al. [29] reported flexural strengths of 219 and 198 MPa for longitudinally printed and transversely printed samples, respectively. This effect is hypothesized to be small for CODE as no printing flaw was observed in the samples and no visible differences in cross-sections and microstructures of samples cut in different directions were identified. However, further evidence is required to confirm this hypothesis. Note that for other AM processes, the highest values reported in each reference are given in for comparison.

Table 4 shows that the CODE process has a very good standing among AM processes in terms of mechanical properties. This is due to several facts including:

- fine alumina powder facilitating the sintering process,
- high solids loading paste resulting in a dense green body,
- printing at room temperature as opposed to high temperature or low temperature which may cause clogging of the nozzle as a result of paste drying or freezing,
- optimal partial drying during the printing process with the aid of an infrared lamp, which enables strong bonding between layers,
- uniform partial drying during the printing process with the aid of an oil bath surrounding the part, which precludes crack formation, warpage, and moisture/temperature gradient in the part,
- employing a new extrusion mechanism, which guarantees consistent flowrate and avoids pores in the part, and
- use of humid drying to remove water content after part fabrication which increases the green body density

Other advantages of the CODE process include low cost and simplicity of feedstock preparation, fabrication system and post-processing; potential for fabricating functionally graded materials via mixing two or more pastes of different materials at varying rates; capability of embedding sensors or other components during the fabrication process as demonstrated in [32]; and use of water as the liquid medium in the paste which facilities efficient post-processing and enables fabrication of large solid components (mainly because water can be more readily removed). However, the CODE process has two main limitations: 1) significant staircase effect; and 2) difficulty in fabricating fine features in complex parts. These limitations could be alleviated by employing finer extrusion nozzles (up to ~150 μm diameter) which, on the other hand, would increase the fabrication time. Adaptive slicing [33] and adaptive rastering [34] techniques have been proposed to minimize the fabrication time when finer diameter nozzles are used.

4. Conclusions

Properties of advanced ceramic parts produced by a novel additive manufacturing process called the Ceramic On-Demand Extrusion (CODE) process have been characterized extensively in this paper. Thirty Al_2O_3 test bars were fabricated using the CODE process to examine the properties of

the produced parts after sintering. The specimens had a relative density of 98%, a Young's modulus of 371±14 GPa, an unbiased Weibull modulus of 7.85, an average flexural strength of 364±50 MPa, a fracture toughness of 4.5±0.1 MPa•$m^{0.5}$, and a hardness of 19.8±0.6 GPa. These properties surpass those produced by most other additive manufacturing processes and match those produced by conventional fabrication techniques. This indicates the high potential of the CODE process to be employed in industrial applications, especially where one-of-a-kind parts or a small number of customizable products with good mechanical properties are needed.

Acknowledgements

The authors gratefully acknowledge the financial support by the National Energy Technology Laboratory of the U.S. Department of Energy's Office of Fossil Energy under the contract DE-FE0012272, as well as the Intelligent Systems Center at the Missouri University of Science and Technology.

References

1. Griffin EA, McMillin S. Selective laser sintering and fused deposition modeling processes for functional ceramic parts. In: *Solid Freeform Fabrication Symposium*. Austin, TX, USA; 1995:25-30.
2. Griffith ML, Halloran JW. Freeform fabrication of ceramics via stereolithography. *J Am Ceram Soc*. 1996;79(10):2601-2608. doi:10.1111/j.1151-2916.1996.tb09022.x.
3. Grau J, Moon J, Uhland S, Cima MJ, Sachs E. High green density ceramic components fabricated by the slurry-based 3DP process. In: *Solid Freeform Fabrication Symposium*. Austin, TX, USA; 1997:371-378.
4. Noguera R, Lejeune M, Chartier T. 3D fine scale ceramic components formed by ink-jet prototyping process. *J Eur Ceram Soc*. 2005;25(12):2055-2059. doi:10.1016/j.jeurceramsoc.2005.03.223.
5. Griffin C, Daufenbach J, McMillin S. Desktop manufacturing: LOM vs pressing. *Am Ceram Soc Bull*. 1994;73(8):109-113.
6. Danforth SC. Fused deposition of ceramics: a new technique for the rapid fabrication of ceramic components. *Mater Technol*. 1995;10(7-8):144-146.

7. Stuffle K, Mulligan A, Calvert P, Lombardi J. Solid freebody forming of ceramics from polymerizable slurry. In: *Solid Freeform Fabrication Symposium*. Austin, TX, USA; 1993:60-63.

8. Cesarano III J, Segalmen R, Calvert P. Robocasting provides moldless fabrication from slurry deposition. *Ceram Ind*. 1998;148:94-102.

9. Huang T, Mason MS, Hilmas GE, Leu MC. Freeze-form extrusion fabrication of ceramics. In: *Solid Freeform Fabrication Symposium*. Austin, TX, USA; 2005:73-85.

10. Travitzky N, Bonet A, Dermeik B, et al. Additive manufacturing of ceramic-based materials. *Adv Eng Mater*. 2014;16(6):729-754. doi:10.1002/adem.201400097.

11. Chen F, Cao F, Pan H, et al. Mechanical and dielectric properties of silicon nitride ceramics with high and hierarchical porosity. *Mater Des*. 2012;40:562-566. doi:10.1016/j.matdes.2012.03.026.

12. Zocca A, Colombo P, Gomes CM, Günster J. Additive manufacturing of ceramics: issues, potentialities, and opportunities. *J Am Ceram Soc*. 2015;98(7):1983-2001. doi:10.1111/jace.13700.

13. Ghazanfari A, Li W, Leu MC, Hilmas GE. A novel extrusion-based additive manufacturing process for ceramic parts. In: Bourell DL, Crawford RH, Seepersad CC, Beaman JJ, Fish S, Marcus H, eds. *Solid Freeform Fabrication Symposium*. Austin, TX, USA; 2016:1509-1529.

14. Zomorodi H, Landers RG. Extrusion based additive manufacturing using explicit model predictive control. In: *American Control Conference*. Boston, MA, USA; 2016:1747-1752.

15. ASTM C1161. *Standard Test Method for Flexural Strength of Advanced Ceramics at Ambient Temperatures*. West Conshohocken, PA, USA; 2013. doi:10.1520/C1161-13.

16. ASTM C1239. *Standard Practice for Reporting Uniaxial Strength Data and Estimating Weibull Distribution Parameters for Advanced Ceramics*. West Conshohocken, PA, USA; 2013. doi:10.1520/C1239-13.

17. ASTM C1421. *Standard Test Methods for Determination of Fracture Toughness of Advanced Ceramics*. West Conshohocken, PA, USA; 2010. doi:10.1520/C1421-10.

18. ASTM C1327. *Standard Test Method for Vickers Indentation Hardness of Advanced Ceramics*. West Conshohocken, PA, USA; 2015. doi:10.1520/C1327-15.

19. Sadd MH. *Elasticity: Theory, Applications, and Numerics*. second edi. Burlington, MA, USA: Elsevier; 2009.

20. Boch P, Niepce JC, eds. *Ceramic Materials: Processes, Properties and Applications*. 1st ed. Newport Beach, CA, USA: ISTE USA; 2007.

21. Brook RJ, ed. *Concise Encyclopedia of Advanced Ceramic Materials*. 1st ed. Elmsford, NY, USA: Pergamon Press; 1991.

22. Auerkari P. *Mechanical and Physical Properties of Engineering Alumina Ceramics*. Vol 1792. Vuorimiehentie, Finland; 1996.

23. ASTM C1322. *Standard Practice for Fractography and Characterization of Fracture Origins in Advanced Ceramics*. West Conshohocken, PA, USA; 2010. doi:10.1520/C1322-05BR10.

24. ASTM C1683. *Standard Practice for Size Scaling of Tensile Strengths Using Weibull Statistics for Advanced Ceramics*. West Conshohocken, PA, USA; 2015. doi:10.1520/C1683-10R15.

25. Schwentenwein M, Homa J. Additive manufacturing of dense alumina ceramics. *Int J Appl Ceram Technol*. 2015;12(1):1-7. doi:10.1111/ijac.12319.

26. Liu ZH, Nolte JJ, Packard JI, Hilmas G, Dogan F, Leu MC. Selective laser sintering of high-density alumina ceramic parts. In: Hinduja S, Fan K-C, eds. *Proceedings of the 35th International MATADOR Conference*. Vol 3. Taipei, Taiwan: Springer; 2007:351-354. doi:10.1007/978-1-84628-988-0_79.

27. Feilden E, Blanca EG-T, Giuliani F, Saiz E, Vandeperre L. Robocasting of structural ceramic parts with hydrogel inks. *J Eur Ceram Soc*. 2016;36(10):2525-2533. doi:10.1016/j.jeurceramsoc.2016.03.001.

28. Li J, Leu MC, Hilmas GE. Effects of temperature on aqueous freeform extrusion fabrication. In: Bourell D, Beaman J, Crawford R, Fish S, Marcus H, Seepersad C, eds. *Solid Freeform Fabrication Symposium*. Austin, TX, USA; 2015:319-331.

29. Huang T, Mason MS, Zhao X, Hilmas GE, Leu MC. Aqueous-based freeze-form extrusion fabrication of alumina components. *Rapid Prototyp J*. 2009;15(2):88-95.

30. Maleksaeedi S, Eng H, Wiria FE, Ha TMH, He Z. Property enhancement of 3D-printed alumina ceramics using vacuum infiltration. *J Mater Process Technol*. 2014;214(7):1301-

1306. doi:10.1016/j.jmatprotec.2014.01.019.

31. Gonzalez JA, Mireles J, Lin Y, Wicker RB. Characterization of ceramic components fabricated using binder jetting additive manufacturing technology. *Ceram Int*. 2016;42(9):1-7. doi:10.1016/j.ceramint.2016.03.079.

32. Ghazanfari A, Li W, Leu MC, Zhuang Y, Huang J. Advanced ceramic components with embedded sapphire optical fiber sensors for high temperature applications. *Mater Des*. 2016;112:197-206. doi:10.1016/j.matdes.2016.09.074.

33. Dolenc A, Makela I. Slicing procedures for layered manufacturing techniques. *Comput Des*. 1994;26(2):119–126.

34. Ghazanfari A, Li W, Leu MC. Adaptive rastering algorithm for freeform extrusion fabrication processes. *Virtual Phys Prototyp*. 2015;10(3):163-172. doi:10.1080/17452759.2015.1096798.

Figure 1. Schematic of the Ceramic On-Demand Extrusion process.

Figure 2. Test bars during the CODE process.

Figure 3. Fully articulating test fixture and deflectometer.

Figure 4. SEM image showing a typical microstructure of the Al_2O_3 produced via the CODE process.

Figure 5. Weibull plot of the flexural strength data from Al_2O_3 test specimens.

Figure 6. Typical fracture surface (a) and indented surface (b).

Figure 7. A typical cross-section under SEM showing a solid surface with no flaws.

Figure 8. Two typical fracture origins near the tensile surface of the Al_2O_3 flexure test specimens.

Table 1. Powder properties.

Name	Particle Size (μm)	Surface Area (m^2/g)	Purity
Al_2O_3 (A-16SG)	0.34	9.44	99.8%

Table 2. Printing parameters used in the CODE process to fabricate test bars.

Nozzle diameter (μm)	610
Nozzle travel speed (mm/s)	30
Layer thickness (μm)	400
Number of layers	14
Line spacing (μm)	600
Number of lines in a layer	13
Lamp distance (m)	0.25
Radiation time (s)	30

Table 3. Amount of shrinkage and relative densities of parts at each stage.

	Size (mm)	**Linear shrinkage (%)**	**Volumetric shrinkage (%)**	**Relative density (%)**
As-printed	72.0×7.8×5.6	-	-	57*
Dried	71.0×7.5×5.4	1.4×3.8×3.6	8.6	62*
Sintered	62.8×6.3×4.6	12.8×19.2×17.9	42.1	98

* These densities are calculated by dividing mass of alumina powder by volume of the part.

Table 4. Mechanical properties of alumina parts produced by different additive manufacturing processes.

Process	**Relative density (%)**	**Young's modulus (GPa)**	**Flexural strength (MPa)**	**Characteristic strength (MPa)**	**Weibull modulus**	**Fracture toughness ($MPa \cdot m^{0.5}$)**	**Hardness (GPa)**	**2c (μm) assuming long flaws**	**2c (μm) assuming round flaws**
CODE	98	371±14	364±50	385.3	8.3×0.943	4.5±0.1	19.8±0.6	102±34	252±84
LCM [25]	99	-	369*-383*	-	11.2×0.955	-	-	-	-
SLS [26]	88	-	255±17	-	-	-	-	-	-
RC** [27]	97	-	236*-248*	297	8.9×0.901	3.3±0.2	18.6±0.8	89	218
FEF** [28,29]	87-92	327±20	219	-	5.4×0.947	-	14.4±0.9	-	-
3DP**,† [30]	85	-	62	-	-	-	-	-	-
BJ** [31]	-	54±14.5	Very low‡	-	-	-	1.5±0.01	-	-

* Original value converted to standard "B" bar using equations (6) and (7) for fair comparison.

** Highest values in the paper are reported here.

† Vacuum infiltration was used to enhance the mechanical properties.

[‡] The compressive strength was only 132 MPa, so the flexural strength was minimal.

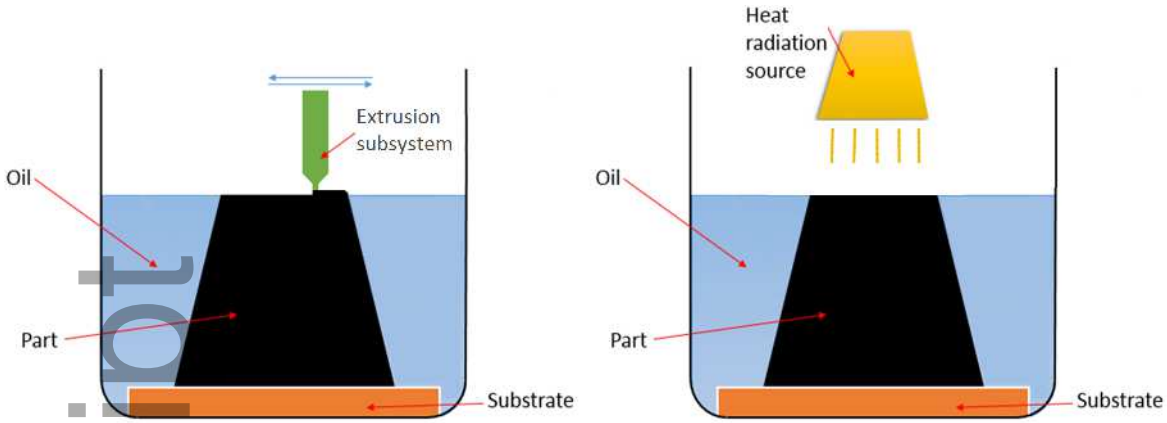

ijac_12665_f1.tif

ijac_12665_f2.tif

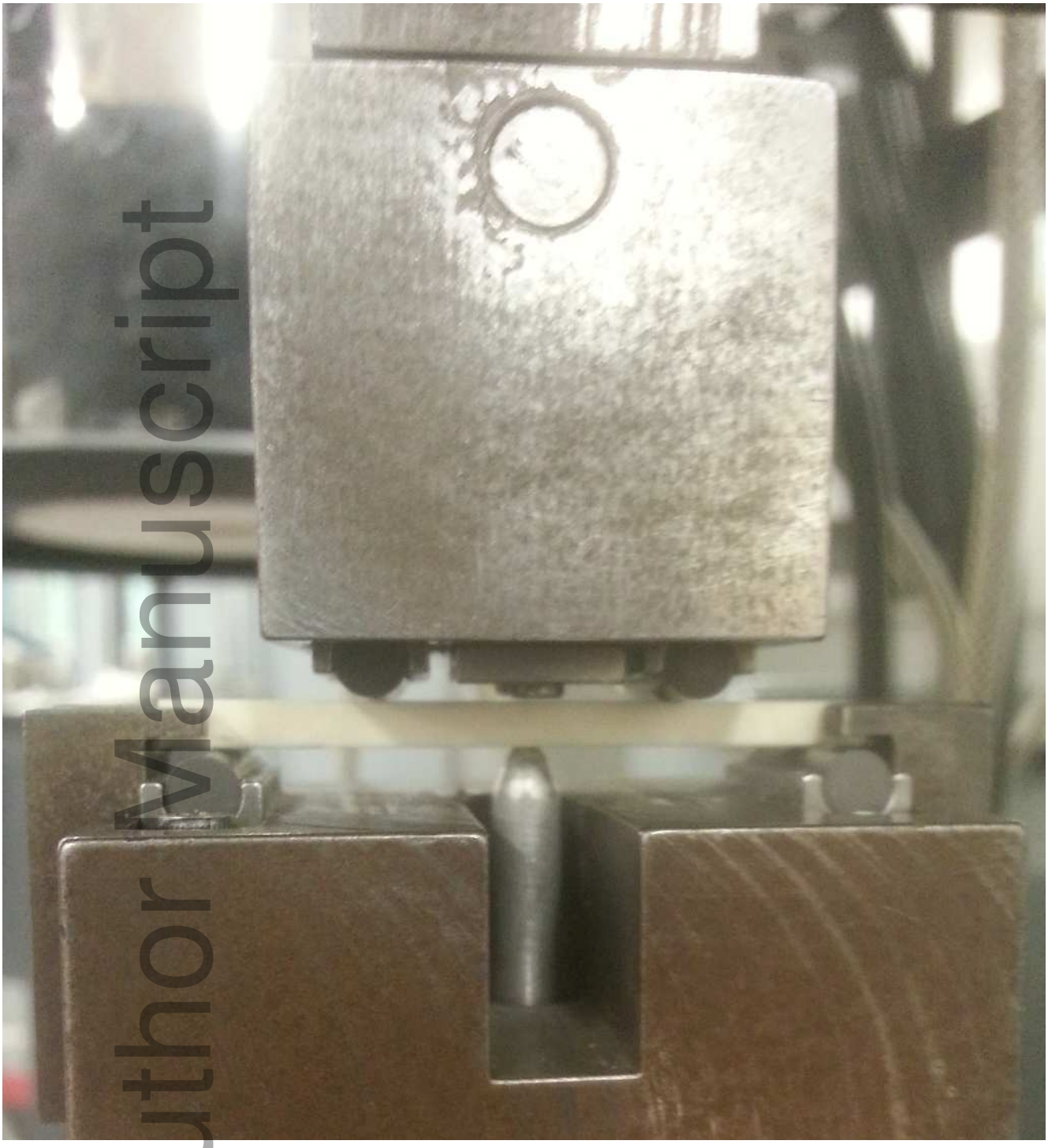

ijac_12665_f3.tif

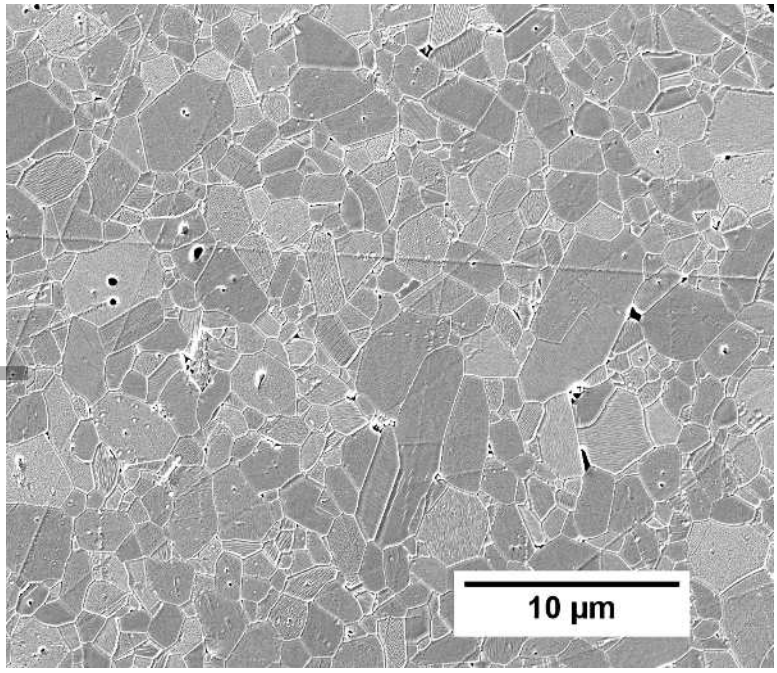

ijac_12665_f4.tif

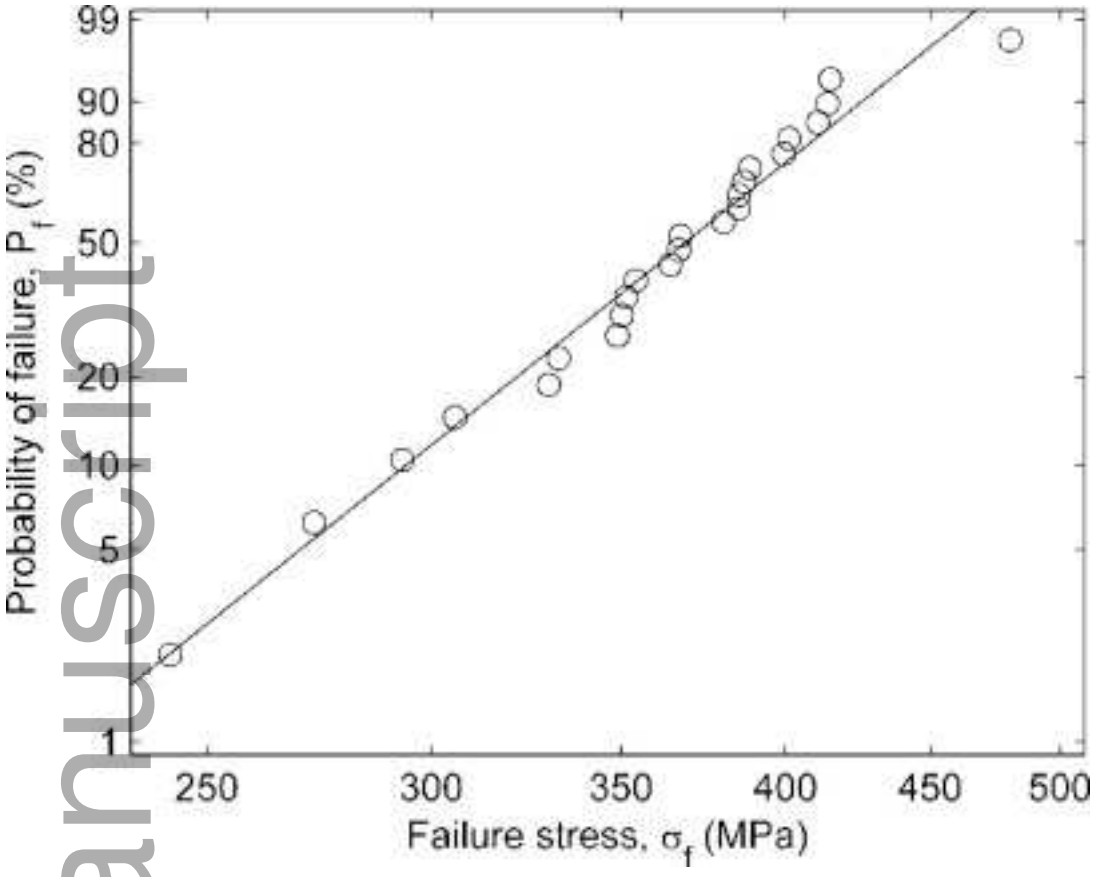

ijac_12665_f5.tif

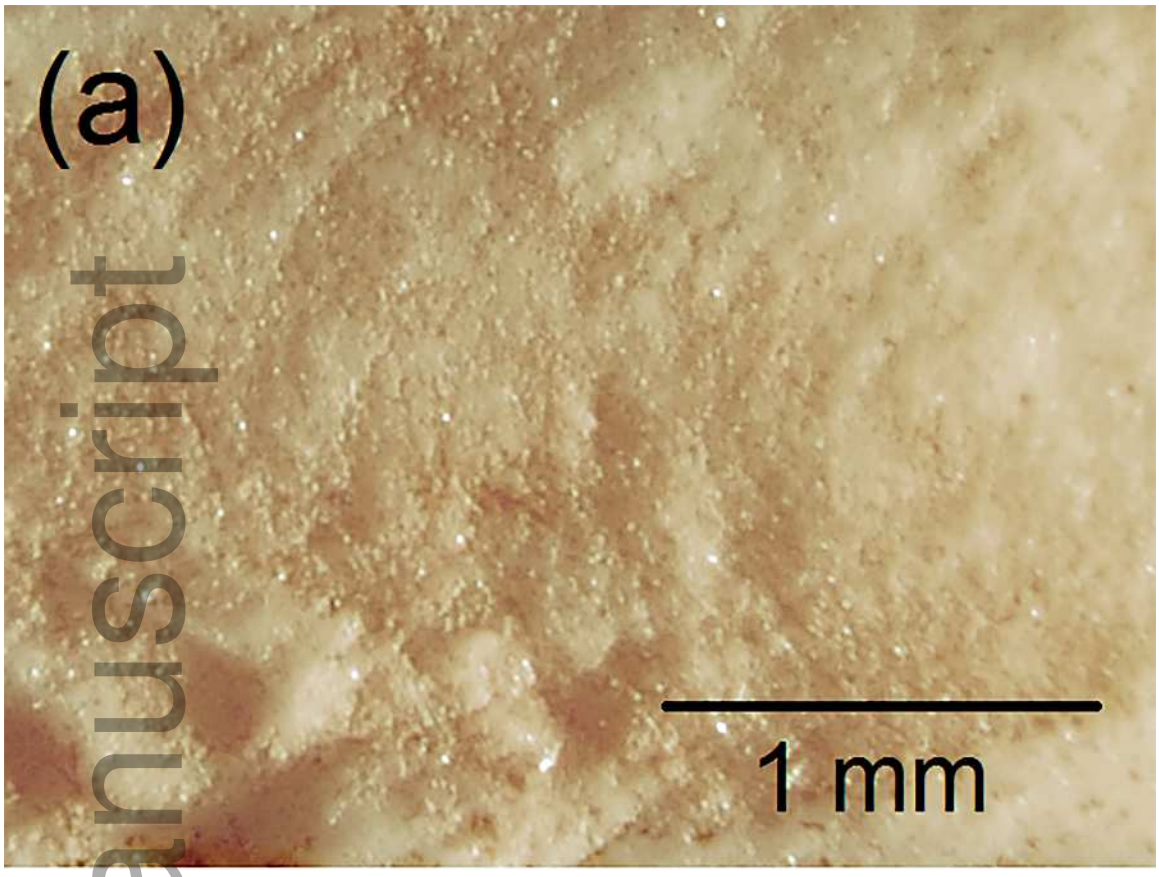

ijac_12665_f6a.tif

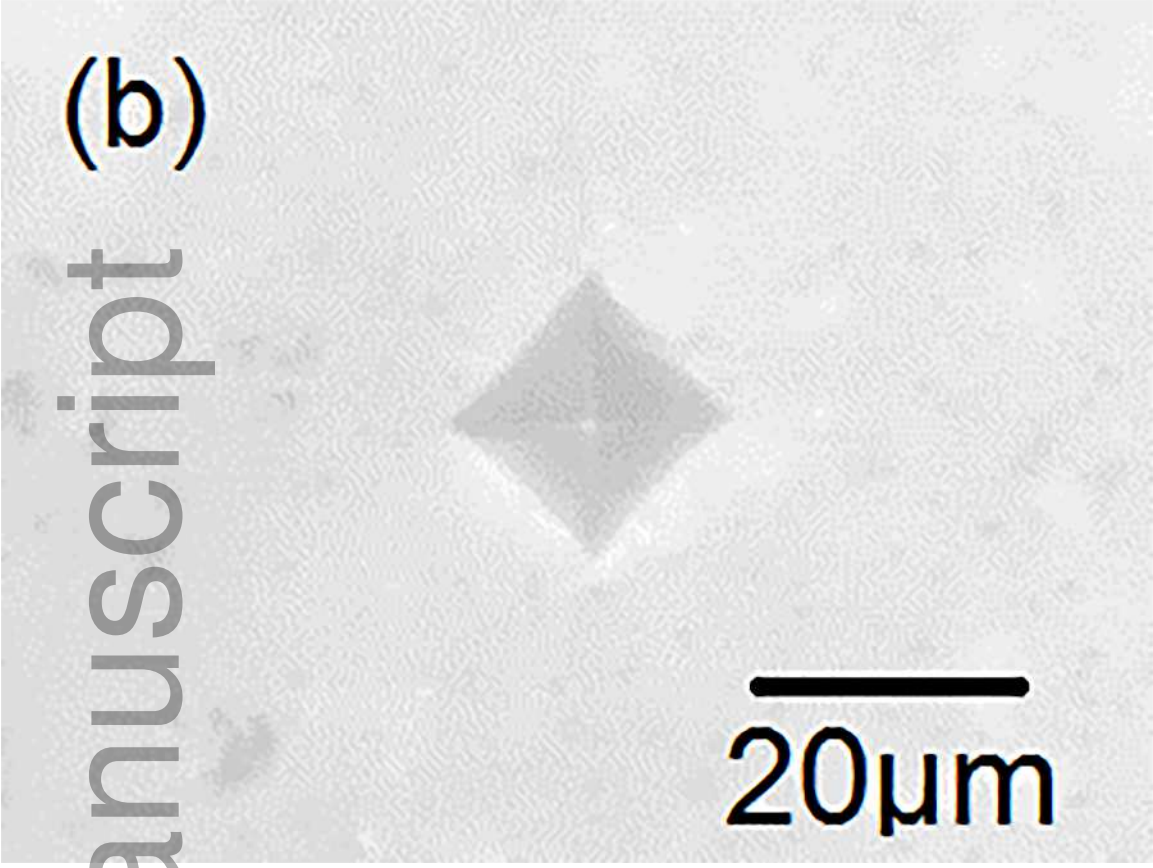

ijac_12665_f6b.tif

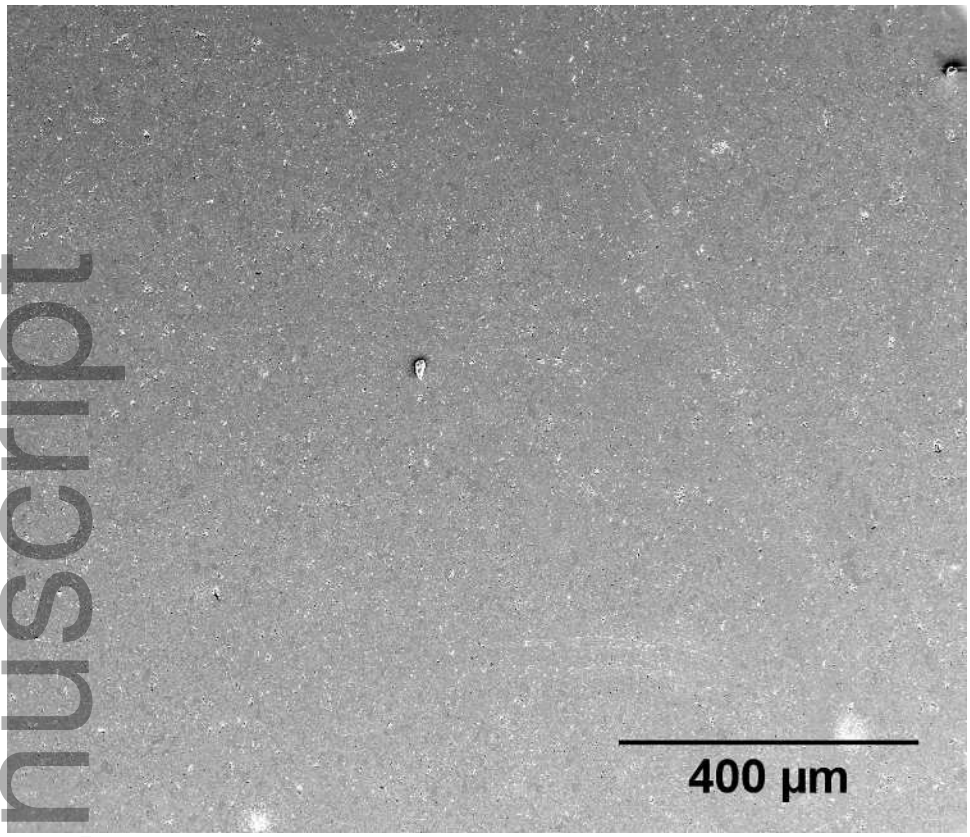

ijac_12665_f7.tif

ijac_12665_f8a.tif

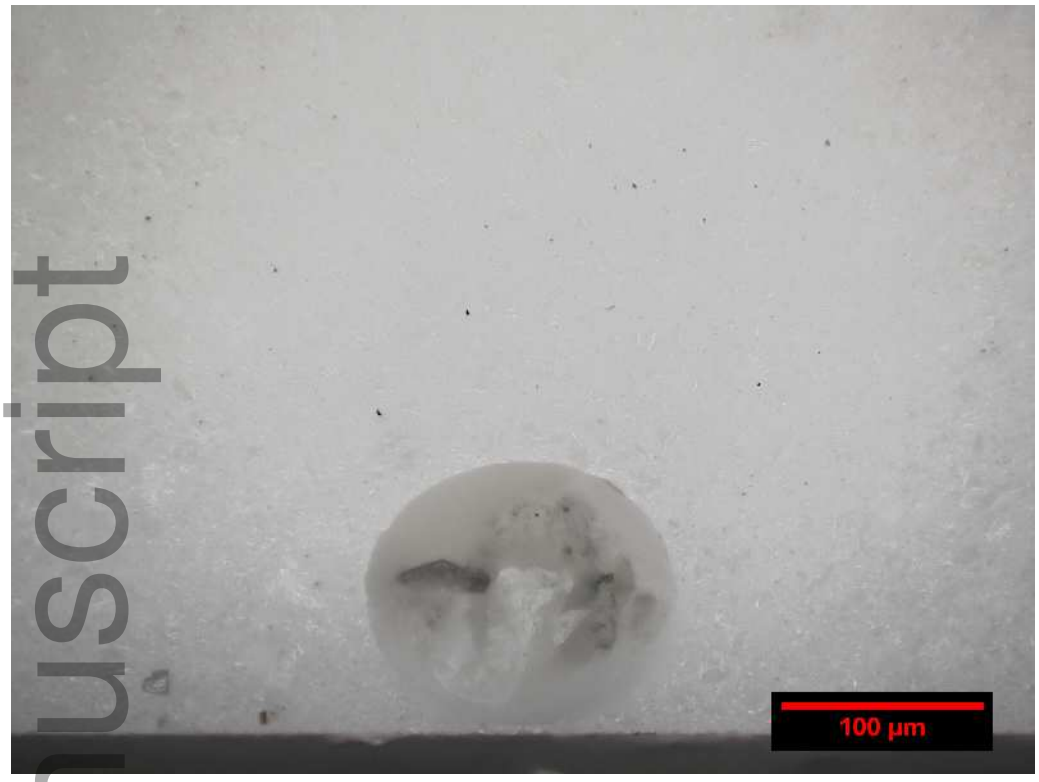

ijac_12665_f8b.tif